Verification of effect of secondary conductor bar on starting characteristics in line-start type self-excited wound-field synchronous motor

IET Electric Power Applications

Research Article

IET Journals
The Institution of Engineering and Technology

Verification of effect of secondary conductor bar on starting characteristics in line-start type self-excited wound-field synchronous motor

ISSN 1751-8660
Received on 19th June 2020
Revised 17th November 2020
Accepted on 15th December 2020
doi: 10.1049/iet-epa.2020.0497
www.ietdl.org

Masahiro Aoyama[1] ✉, *Takahiro Mizuta*[2], *Kazumasa Ito*[2]

[1]*Electrical and Electronics Engineering, Shizuoka University, 3-5-1 Johoku, Naka-ku, Hamamatsu, Japan*

[2]*Advanced Technology R&D Centre, Mitsubishi Electric Corporation, 8-1-1, Tsukaguchi Honmachi, Amagasaki, Hyogo, Japan*

✉ *E-mail: aoyama.masahiro@shziuoka.ac.jp*

Abstract: This study clarifies experimentally the effect of the secondary conductor bar on line-start characteristics in a line-start type self-excited wound-field synchronous motor. This motor is based on a brushless wound-field synchronous motor having a rotor winding connected to a diode rectifier circuit. And it has a secondary conductor bar that is independently connected at a pitch of one pole, without end-ring. First, the operation principle of the proposed motor and its magnetic circuit design are described, and then the details of the prototype for principle verification are clarified. Next, when the combination of the connecting of the secondary conductor bar is changed, an experiment of line-starting characteristics and measured rotor field current is demonstrated. Consequently, it was clarified that the influence on the synchronous pull-in, speed ripple, and rotor field current.

1 Introduction

An induction motor (IM) is widely used today as electric motors for driving fans or pumps in industrial applications [1]. In an application that rotates at a constant speed and does not require a variable speed operation, the cost advantage of an IM that can be directly connected to a commercial power supply and driven directly is great. However, the IM is required to supply the field magnetic flux from the primary side in principle, and there is a problem that it is difficult to improve efficiency in terms of power factor and efficiency. In order to improve performance, research and development has been conducted to reduce secondary resistance by using high-performance magnetic materials, adding silver paste to the secondary conductor bar, and using a copper squirrel cage. On the other hand, the magnetic circuit of the IM does not change from the generally known squirrel cage structure. By the way, the permanent magnet type synchronous motor (PMSM), which can be said to be synonymous with high-efficiency and high-performance motor, it is a very excellent machine with high efficiency, power factor, and torque density, but it requires an inverter to drive in synchronously.

In view of the above, in recent years, two new types of research and development have been actively reported mainly to improve the performance of line-start type motors. One is a structure in which a secondary conductor bar is embedded on the outer diameter side of the rotor based on the structure of a PMSM. These motors are named line-start type PMSMs (LS-PMSMs) [2–12]. It consists of a combination of an IM and an embedded PMSM. When the AC power is directly supplied, induction torque is generated in the secondary conductor bar due to the slip frequency and rotation of the rotor is accelerated. Then, the permanent magnet flux embedded in the rotor is synchronised with the rotating magnetic field, so that synchronous pulling can be performed. By driving according to the above principle, the problem of the magnet type synchronous machine which cannot start rotating by itself is solved, and high torque with high-efficiency driving becomes possible during the synchronous speed drive. On the other hand, during asynchronous rotation up to the synchronous speed, the AC magnetic flux link to the magnets, so that eddy current loss occurs in the magnets. As a result, it becomes necessary to design a magnetic circuit that avoids the risk of demagnetisation, such as by using a magnet with a high coercive force [10]. Furthermore, when the rotor rotates under asynchronisation, braking torque is generated due to the magnetic flux of the magnets, which deteriorates the starting characteristics [7].

The other type is a line-start type synchronous reluctance motor (LS-SynRM) [13–21]. This motor is based on the structure of a reluctance motor having a multi-layer flux barrier and has a structure in which a secondary conductor bar is embedded at an appropriate position in the flux barrier. Similar to the former LS-PMSM, after directly power supply, the secondary conductor bars embedded in the flux barrier generate induction torque from the slip frequency and begin the self-rotation. After accelerating to the synchronous speed, the reluctance torque is generated by the permeance distribution of the flux barrier formed in the rotor, so that the rotor can be driven synchronously. Since synchronous driving is possible, secondary copper loss in the secondary conductor bar can be reduced during synchronisation. On the other hand, compared to the LS-PMSM, the torque density is lower. As a design constraint, it is difficult to achieve without a distributed winding stator. Therefore, it is difficult to reduce armature copper loss.

To drawback these background problems, the authors are researching a third new type of line-start type motor [22]. This technique is classified as a brushless wound-field synchronous motor that obtains the rotor magnetomotive force from the armature side by the self-excitation. For the brushless wound-field, a technique using an embedded exciter, or a rotating thyristor has been reported [23–26]. These are excellent technologies for a large grid-connected synchronous machine, but there are also problems of increasing the size of the machine due to the need for the exciter for applications that require miniaturisation. A doubly-fed technique has also been reported in which secondary excitation is performed on the rotor side from two different frequency rotating magnetic fields [27, 28]. In the case of this technique, there is a possibility of a high-power factor than IM. On the other hand, since two types of armature windings are required, there is concern about the increase in armature copper loss. In recent years, the new brushless wound-field technique has also been proposed. It is a technique that uses the magnetic modulation principle by the rotor salient poles by generating a rotating magnetic field and a static magnetic field from the armature side [29].

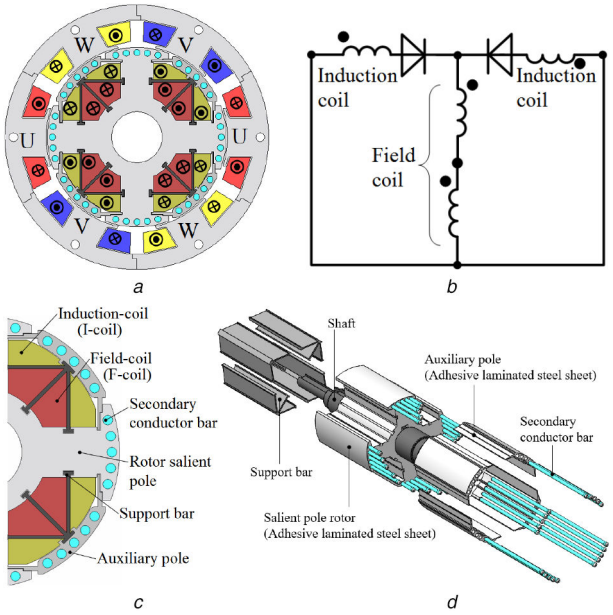

Fig. 1 *Proposed motor and rotor winding circuit*
(a) Radial cross-section diagram, ***(b)*** Rotor winding rectifier circuit, ***(c)*** Rotor components, ***(d)*** Rotor structure

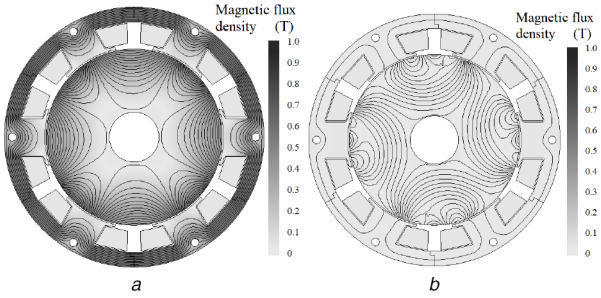

Fig. 2 *Harmonic magnetic flux distribution generated by the concentrated winding stator*
(a) Third time-harmonic, ***(b)*** Sixth time-harmonic

As a brushless wound-field technique for applications where self-starting is desired, this paper proposes a line-start type self-excited technique utilising space harmonics. As a proposal, a structure of wound-field type synchronous motor having a concentrated winding stator structure and capable of self-starting with brushless power supply is being studied. The features of this motor are a concentrated winding stator structure that can reduce armature copper loss and a structure that can form field poles in the rotor without using permanent magnets. Secondary conductor bars are provided on the outer circumference of the rotor for self-rotation. As a magnetic circuit, the IM and the self-excited wound-field type synchronous motor are integrated. First, this paper describes the operation principle of the proposed motor. Then, the performance of the proposed motor depending on the combination of the secondary conductor bar connection will be demonstrated. Therefore, this paper reports on the starting characteristics when the connection of the secondary conductor bar was changed using a prototype, and the results were clarified.

2 Line-start type self-excited wound-field synchronous motor

2.1 Operation principle

Fig. 1*a* shows a radial cross-section of the proposed motor. It has a three-phase concentrated winding stator structure, and the rotor structure has a major feature. The rotor has salient poles and is composed of two types of windings, an induction coil (I-coil) and a field coil (F-coil). Although details will be described later, the I-coil generates an electromotive force from the harmonic flux, and the F-coil plays a role of forming a field pole through the diode. These windings are wound around the salient poles. The rotor windings are diode-rectified circuit-connected on the rotor as shown in Fig. 1*b*. In addition, as shown in Figs. 1*c* and *d*, 40 secondary conductor bars are embedded in the outer circumference of the rotor. And, for the reason to be described later, it is short-circuited at the pole pitch, unlike the conventional general all-short-circuited squirrel cage type. The auxiliary pole is set for the purpose of interlinking a large amount of harmonic flux with the I-coil and to prevent the centrifugal force of the rotor windings.

First, the diode rectifier circuit connected to the rotor winding will be described in detail. The self-excitation technique utilising space harmonics described below is based on the past research results of one of the authors [30]. Fig. 2 shows the distributions of the third- and sixth-order time-harmonic when a three-phase sinusoidal excitation is performed on a concentrated winding stator with a circular laminated steel plate rotor. Here, JMAG Designer *ver.* 18 from JSOL, Japan was used for electromagnetic field analysis. The simulation was carried out by the transient state solver of the finite element method. The power supply was a three-phase voltage source, and a two-dimensional model was used. The harmonic analysis of Fig. 2 was carried out using the magnetic flux distribution separation function for each frequency in the time domain. The FE-analysis results shown in this paper are calculated using the resistance values measured by the prototype, which will be described later. The eddy currents of the bars are obtained from the interlinking magnetic flux by defining the electrical resistivity. Similarly, the inductance of the bars is taken into consideration by internal computation by JMAG's FEM function above. However, the bar connection parts are given by the resistor and its inductance is not taken into consideration. As shown in this figure, it can be confirmed that particularly many second-order space harmonics occur. Then, why large third-time harmonics are generated is explained below. Fig. 3 shows a theoretical magnetic flux

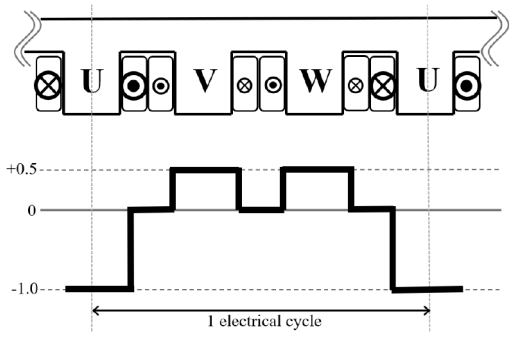

Fig. 3 *Theoretical magnetic flux waveform at U-phase current maximum*

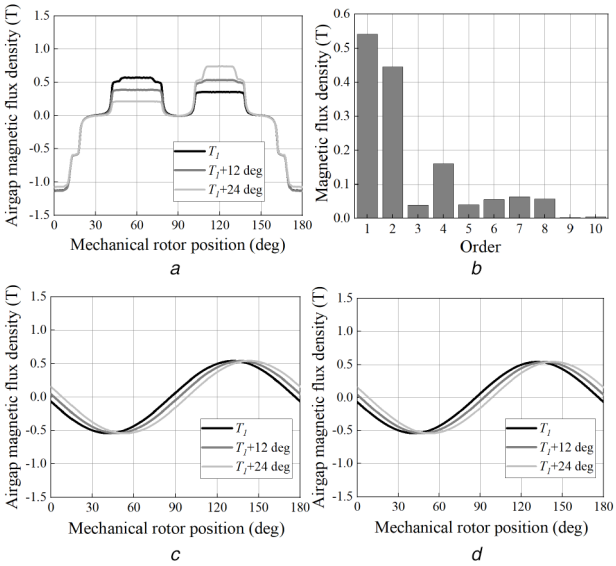

Fig. 4 *Simulated magnetic flux density waveform with a circular laminated steel plate rotor*
(a) Airgap magnetic flux density waveforms, ***(b)*** Harmonic contents at T_1 of (a), ***(c)*** Fundamental component of airgap magnetic flux density, ***(d)*** Second-order component of airgap magnetic flux density

distribution when the U-phase current is maximum in a three-phase concentrated winding stator with a three-phase balanced state.

When normalised by the maximum magnetic flux density, the U-phase is −1.0 and V and W phases are +0.5, as shown in this figure. Since it is asymmetric with respect to the x-axis, it is confirmed that large second-order harmonic are superposed. Similarly, Fig. 4*a* shows the results of obtaining the gap magnetic flux density waveform by FE-analysis. Fig. 4*b* shows the results of harmonic analysis of this waveform. Here, in order to confirm the temporal change of the harmonics superposed on the fundamental waveform, the waveforms when the electrical angle advances by 12° and 24° with respect to the reference time T_1 are also shown, when it is approximated up to the second-order, it becomes as shown in Figs. 4*c* and *d*. From these results, the following two points should be paid special attention to here. The first point is that, despite the sinusoidal excitation, the second space harmonic with an amplitude of about 82% with respect to the fundamental magnetic flux is inevitably generated due to the magnetic circuit configuration of the concentrated winding stator. The second point is that the second space harmonic temporally moves in the opposite direction to the moving direction of the fundamental flux. Mathematically expressing it, when a three-phase sinusoidal current (I_u, I_v and I_w) and the armature magnetomotive force F_s are given by the following equations:

$$\begin{cases} I_u = I_a\cos(\omega t - \delta) \\ I_v = I_a\cos\left(\omega t - \frac{2}{3}\pi - \delta\right) \\ I_w = I_a\cos\left(\omega t - \frac{4}{3}\pi - \delta\right) \end{cases} \tag{1}$$

$$F_s(t,\theta) = N\begin{Bmatrix} I_u R_s(\theta) + I_v R_s\left(\theta - \frac{2}{3}\pi\right) \\ +I_w R_s\left(\theta - \frac{4}{3}\pi\right) \end{Bmatrix} \tag{2}$$

Here N is the number of turns of the armature coil, ω is the electrical angular velocity, and δ is the current phase, respectively. R_S means a spatial permeance distribution and is given by the following equation:

$$R_s(\theta) = R_{s1}\cos\theta + R_{s2}\cos(2\theta - \pi) \tag{3}$$

Here, R_{s1} represents the fundamental component, R_{s2} represents the second harmonic component, θ is the spatial rotor position, and the permeance distribution is approximated up to the second order. Furthermore, based on the above results, the second harmonic has an opposite phase to the fundamental waveform. By substituting (1) and (3) into (2) and rearranging, (4) can be obtained as

$$F_s(t,\theta) = \frac{3}{2}NI_a\begin{Bmatrix} R_{s1}\cos(\theta - \omega t + \delta) \\ -R_{s2}\cos(2\theta + \omega t - \delta) \end{Bmatrix} \tag{4}$$

Here, when synchronised with $\theta = \omega t$, (4) can be summarised as follows:

$$F_s(t) = \frac{3}{2}NI_a\{R_{s1}\cos\delta - R_{s2}\cos(3\omega t - \delta)\} \tag{5}$$

From this result, it can be confirmed that the second-order space harmonic that rotate in antiphase become the third time-harmonic when observed from the rotor that rotates in synchronisation.

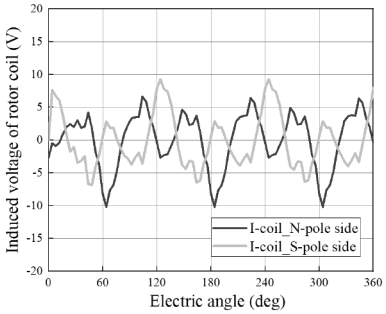

Fig. 5 *Induced voltages of rotor coils*

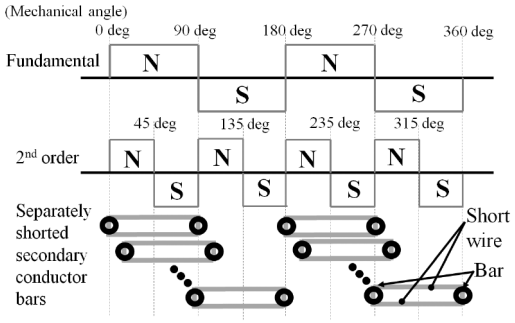

Fig. 6 *Separately shorted secondary conductor bar with pole-pitch*

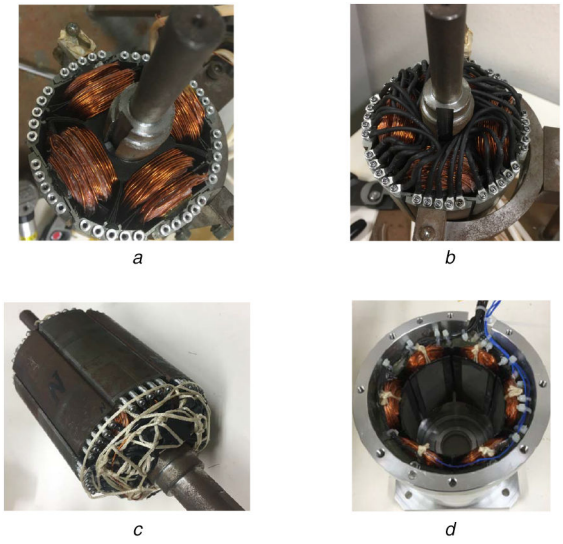

Fig. 7 *Prototype machine*
(a) Rotor windings, ***(b)*** Secondary conductor bar connection, ***(c)*** Rotor assembly, ***(d)*** Stator assembly

Therefore, from this result, the third time-harmonic in Fig. 2*a* could be explained mathematically.

Based on the above, Fig. 5 shows the simulation results of the induced voltages in the proposed motor of Fig. 1 with the rotor winding open. Here, Fig. 5 shows the induced voltages in the I-coil where the F-coil for *N* pole is wound and the I-coil where the F-coil for S pole is wound. From this figure, it can be seen that a third-order induced voltage is generated for one electrical angle cycle. And the phases of the two waveforms are 180° inverted. Therefore, the N-pole side and the S-pole side of the I-coil are connected to the field coil via the cathode rectification via diode rectification as shown in Fig. 1*b*. From the above technique, the field current can be self-excited in the rotor winding by utilising the second-order space harmonic as the field source.

Next, the concept of the secondary conductor bar for self-starting will be described. Under synchronisation, the second-order space harmonic is utilised for self-excitation, so it is desirable that the secondary conductor bar for obtaining starting torque should be not magnetically coupled to the second-order space harmonic during synchronisation. This can be achieved by connecting the secondary conductor bars at the pole pitch as shown in Fig. 6. The short-circuited bars are independent of each other. Here, 40 secondary conductor bars are embedded in the rotor. This number was determined so that the magnetic resistance was high for the sixth harmonic in Fig. 2*b*. Here, the sixth order is not utilised for self-excitation, so it is desirable to reduce it.

2.2 Prototype

Fig. 7 shows the prototype, and Table 1 shows the main specifications of the prototype. From the viewpoint of assemblability, the rotor core, stator core and the auxiliary poles are made of an electromagnetic steel sheet laminated by bonding. A wire diameter of φ0.8 was wound around the salient pole as I-coil and F-coil via 0.5 mm thick insulating bobbin. The space factor of the rotor winding is 21.5% for I-coil and 45.7% for F-coil due to the limitation of the coil-end length and the trial production by hand winding. As the secondary conductor bar connection, as shown in Fig. 7*b*, a wire of φ1.1 was used to connect as shown in Fig. 6. Here, the purpose of this paper is to verify how the starting characteristics change depending on the wiring combination of the secondary conductor bars. In order to carry out that purpose, the

Table 1 Main specifications of the prototype

Parameters	Values	Unit
stator outer diameter	125	mm
stack length	80	mm
air gap length	0.65	mm
armature winding connection	2-parallel, Y-connection	—
number of armature coils	100	turn/tooth
resistance of armature coil	0.84	Ω/tooth
number of induction coils	41	turn/pole
number of field coils	104	turn/pole
resistance of induction coil	0.33 (average)	Ω/pole
resistance of field coil	0.86 (average)	Ω/pole
resistance of secondary conductor bar	0.61	mΩ/bar
operation frequency	60	Hz
nominal applied voltage	200	V_{rms}
rating output power	1.5	kW
rating current density of all windings	8	A/mm^2
rated current of all windings	4.0	A_{rms}

prototype was designed with a structure in which both ends of the aluminium secondary conductor bar were threaded with taps. So, the secondary conductor bar connections can change easily. After assembling the parts, as shown in Fig. 7*c*, the parts were tied with a lacing thread so that the connecting parts would not scatter, and then fixed with epoxy resin. This process improves the resistance to centrifugal force and the insulation between the coil and the iron core. The stator was prototyped with segmented cores to increase the coil space factor, and then assembled as shown in Fig. 7*d*. A wire of φ0.8 was used for armature coil, and it was manually wound through a 0.9 mm insulating bobbin. The space factor of armature coil was 41.5%.

3 Experimental test

3.1 Eddy current brake load

It is very important to understand the effects of the secondary conductor bar on the starting characteristics for the optimum design of the proposed motor. The authors have already verified in [22] that the proposed motor can self-start based on the principle. In this paper, it is clarified experimentally how the starting characteristics are affected by changing the combination of the secondary conductor bar connections with respect to the design of the original model.

An eddy current brake was used as the load. Here, the purpose of this research, as described in Section 1, is to build a technology for next-generation general-purpose motors that use fans and pumps as loads. Therefore, when the magnet excitation type eddy current brake is used as a load, the fluid element can be easily simulated. For the eddy current brake, a rotor yoke was made of carbon steel (S45C material according to Japanese Industrial Standards) and a stator was made of aluminium (A2017 material according to Japanese magnetic Industrial Standards) using a magnet with a residual magnetic flux density $B_r = 180$ mT. The housing of eddy current brake was prototyped using a CFRP 3-D printer (Mark Two, Markforged). Fig. 8*a* shows the experimental setup, and Figs. 8*b* and *c* show the prototype eddy current brake. Fig. 8*d* shows a diagram attached to the motor bench as a load. Since the prototype was made for the purpose of verifying the operation principle, the armature winding inductance is not optimised. Therefore, when the nominal voltage is applied in Table 1, the current density greatly exceeds the rating, so in this paper, the voltage is dropped by the transformer for the experiment.

The wiring combinations of the secondary conductor bar are shown in Figs. 9 and 10. In these figures, with respect to the connection of the proposed motor shown in 'Original', 'Bar-1' is in a state where one central connection is open, and 'Bar-2' is where three central connections are open. 'Bar-3', 'Bar-4', 'Bar-5', and 'Bar-6' have one left end opened, two left ends opened, three left ends opened, and four left ends opened in the rotation direction, respectively. Here, the rotation direction is counterclockwise (CCW). In addition to six ways from 'Bar-1' to 'Bar-6', the experiment was also performed when all the connections were opened. As for the applied voltage, as shown in the test environment in Fig. 8*a*, the output voltage is varied by the transformer. Since this transformer adjusts the voltage by manually turning the handle, the value of the accurate applied voltage uses the value measured by the oscilloscope via the differential probe.

Fig. 11 shows the measured results of the line-start characteristics of the original model when the applied voltage is changed via the transformer. From this figure, when the applied voltage is 108.7 V_{rms}, it cannot be pulled in synchronously, and it rotates asynchronously in the state of slip $s = 0.15$. Here, when the synchronous speed is N_S and the rotation speed is N_R, the slip s is defined as the difference between N_S and N_R divided by N_S. Under this applied voltage condition, the torque ripple also dramatically increases. On the other hand, if the applied voltage exceeds 118.9 V_{rms}, synchronous pull-in becomes possible. Further, in the steady state, the torque ripple also becomes smaller. Figs. 12 and 13 show the line-start characteristics under the average applied voltage are 108 V_{rms} with each secondary conductor bar combination model. From this result, it is shown that the starting torque is the largest because 'Original' has the smallest slip s. On the other hand, 'Without connection' has the largest slip s, it was $s = 0.18$. And the above two models have larger speed ripple than other conditions. In other words, it is equivalent to having a large torque ripple. From these results, the secondary conductor bar contributes to the improvement of starting torque. And, it can be seen that the torque ripple changes depending on the connection of the secondary conductor bar. Since the secondary conductor bars are not connected between the poles, stability problems are concerned. This solution should be issued for the future. Fig. 14 shows the armature current waveforms in the steady state. As an example, the results of 'Original', 'Without connection', and 'Bar-1' are shown. In both models, the amplitude fluctuates due to speed ripple. Fig. 15 shows the results of analysing the harmonics superimposed on the fundamental component. Next, Figs. 16 and 17 show the experimental test results when the average applied voltage was set to 130 V_{rms} by turning the dial of the transformer. Fig. 18 shows the armature current waveforms at this applied voltage and, Fig. 19 shows the harmonic analysis results of the armature current of each model in the steady state. From Figs. 16 and 17, 'Without connection' has a large speed overshoot until it reaches a steady state at the synchronous speed, as compared with other models. In addition, 'Bar-1' and 'Bar-3', which have many secondary bar connections, tend to have smaller speed ripple than other models. From these results, it can be understood that the secondary conductor bar has a function of reducing the overshoot by causing

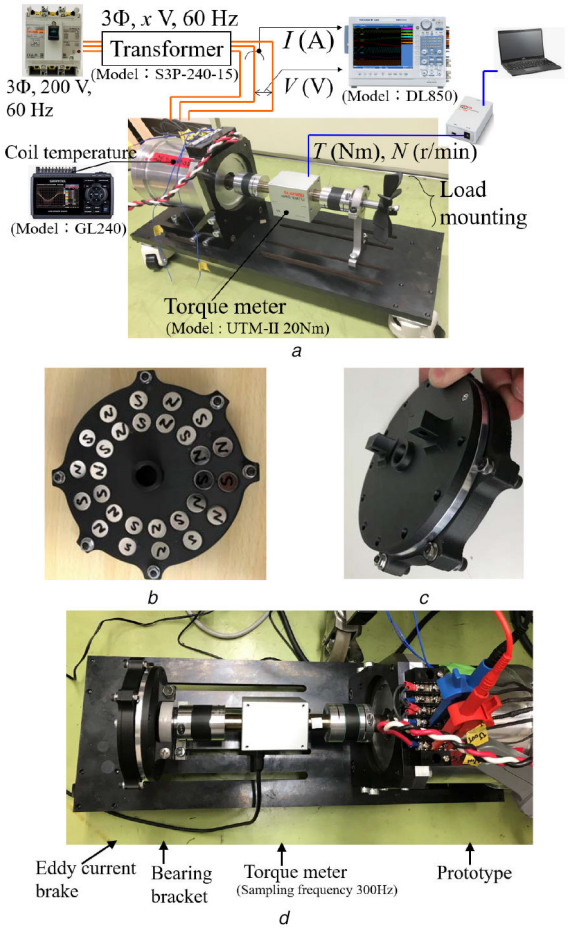

Fig. 8 *Experimental setup*
(a) Measurement setup with propeller type fan load, ***(b)*** Eddy current brake rotor, ***(c)*** Eddy current brake assembly, ***(d)*** Experimental setup with eddy current brake

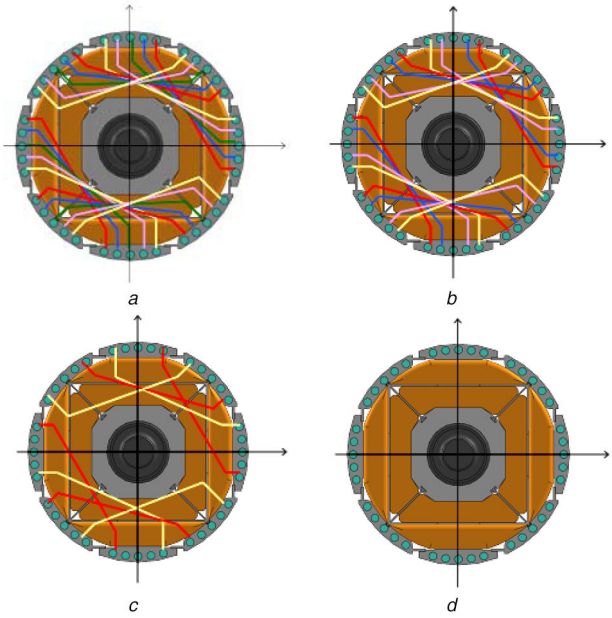

Fig. 9 *Symmetrically changed connection of secondary conductor bar*
(a) Original, ***(b)*** Bar-1, ***(c)*** Bar-2, ***(d)*** Without connection

the slip s to have a negative value and the damping effect against the overshoot exceeding the synchronous speed. Looking at Fig. 19, there is a large variation in the fundamental amplitude of each model. On the other hand, in Fig. 15, there is no significant variation in the fundamental amplitude of each model. Since the armature current is increasing to balance with the load torque, the synchronous torque is decreasing in the model in which the fundamental amplitude of the armature current is large. From this, it can be inferred that the secondary conductor bar affects the synchronous torque. In order to analyse this in more detail, the field current of the prototype is measured and considered in the next section.

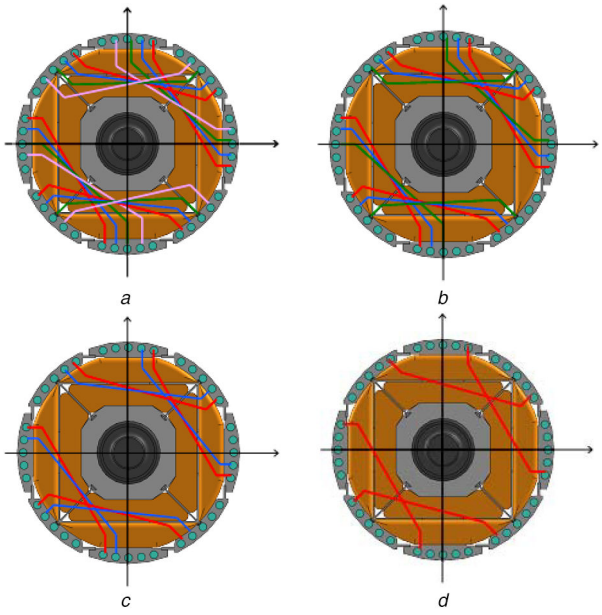

Fig. 10 *Asymmetrically changed connection of secondary conductor bar*
(a) Bar-3, ***(b)*** Bar-4, ***(c)*** Bar-5, ***(d)*** Bar-6

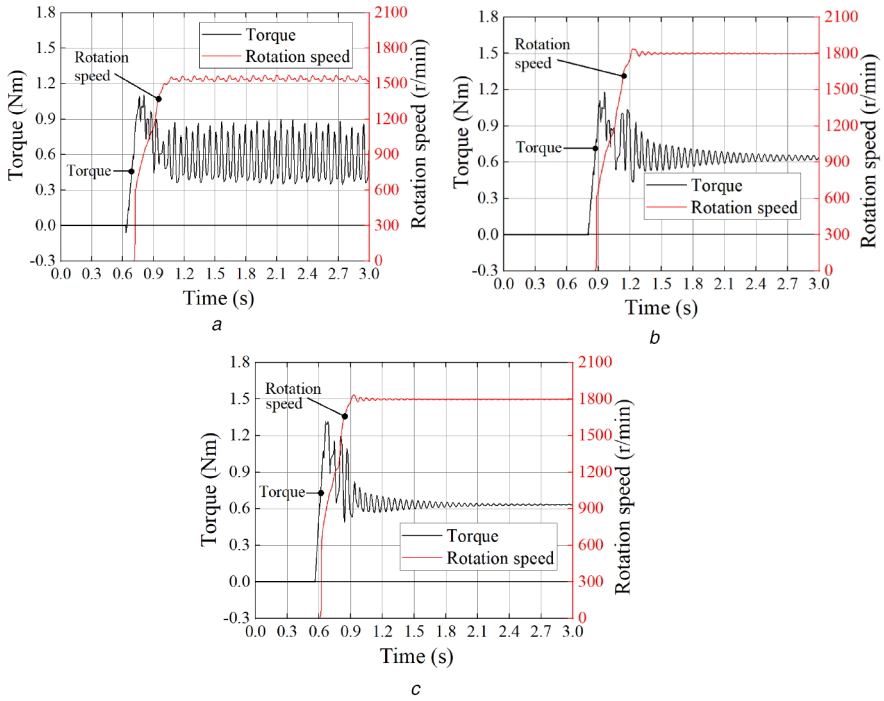

Fig. 11 *Line-start characteristics of original model under eddy current brake load*
(a) Applied voltage at 108.7 V_{rms}, ***(b)*** Applied voltage at 118.9 V_{rms}, ***(c)*** Applied voltage at 128.4 V_{rms}

3.2 Field current measurement

In the previous section, it was clarified experimentally about the effect of the connection of the secondary conductor bar on the starting characteristics. In this section, a deep consideration will be given by experimentally clarifying how the secondary conductor bar affects the self-excited field current. In order to observe the rotor current from the static side, it is necessary to modify the prototype machine with the rectifier circuit mounted on the rotor. First, as shown in Fig. 20, a groove is additionally formed in the shaft, and the rotor winding is dragged to the outside of the bearing through the space between the bearing and its groove. Next, the slip ring wirings and the rotor windings are connected. Those lines are bolted at the relay terminal prototyped with the 3D printer shown in Fig. 20*b*. Furthermore, it will be assembled to the motor bench via the slip ring holder prototyped with a 3D printer. Fig. 20*c* shows the completed rotor current measurement environment. The rotor current measurement setup is incorporated into the measurement system of Fig. 8*a*.

Fig. 21 shows the no-load starting characteristics when the rectifier circuit is connected to the rotor windings or not, and when the secondary conductor bar is connected or not. By comparing Figs. 21*a* and *b*, it is possible to compare the effect of the self-excited field pole on the starting characteristics. In Fig. 21*a*, synchronous pull-in is possible from 102.1 V_{rms}, but in Fig. 21*b*, synchronous pull-in is not possible unless the voltage is increased to 120.0 V_{rms}. This is considered to be because the latter has the rotor rectifier circuit opened and cannot obtain the self-excited electromagnet torque, and therefore the starting characteristics are deteriorated. However, the applied voltage increases and the magnetomotive force increases accordingly, so that the reluctance torque generated by the salient poles can be synchronised. Next, by comparing Figs. 21*a* and *c*, it is possible to compare the effect of the secondary conductor bar on the starting characteristics. From

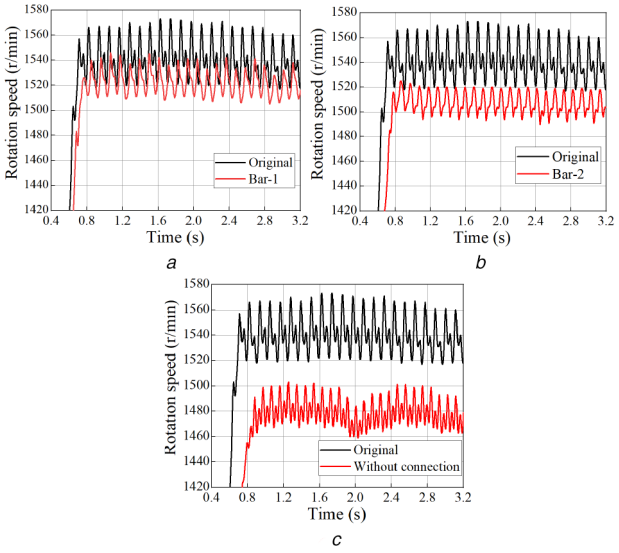

Fig. 12 *Comparison of line-start characteristics with symmetrically changed secondary conductor bar connection under eddy current brake load at average applied voltage 108 V_{rms}*

(a) Original-versus-Bar-1, ***(b)*** Original-versus-Bar-2, ***(c)*** Original-versus-without connection

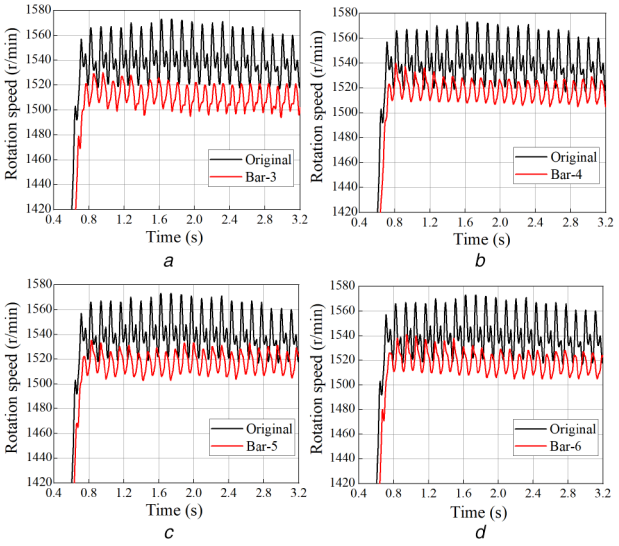

Fig. 13 *Comparison of line-start characteristics with asymmetrically changed secondary conductor bar connection under eddy current brake load at average applied voltage 108 V_{rms}*

(a) Original-versus-Bar-3, ***(b)*** Original-versus-Bar-4, ***(c)*** Original-versus-Bar-5, ***(d)*** Original-versus-Bar-6

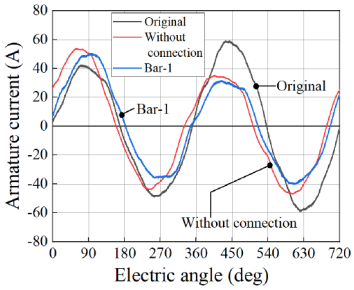

Fig. 14 *Comparison of armature current under eddy current brake load at average applied voltage 108 V_{rms}*

this result, it can be seen that in the case of an extremely light load such as a mechanical loss, self-starting and synchronous pulling can be performed without the secondary conductor bar. This is also clarified in the results of Fig. 21*d*. The reason for this will be discussed in detail later by measuring the rotor field current. Next, by comparing Figs. 21*c* and *d*, it can be seen whether or not the self-starting can be performed even in the state where the field winding and the secondary conductor bar are not connected. This result is very interesting. The starting characteristics have greatly deteriorated, but self-starting is possible. It is asynchronously driven with a slip $s = 0.18$ up to an applied voltage of 120 V_{rms}. When the applied voltage becomes 134 V_{rms}, synchronous pull-in becomes possible. In this prototype, there is no insulation between the aluminium secondary conductor bar and the iron core in which it is embedded. Therefore, it is conceivable that the induction torque may be generated by the generation of the cross-current between the secondary conductor bars through the iron core. When the applied voltage is increased and the magnetomotive force is

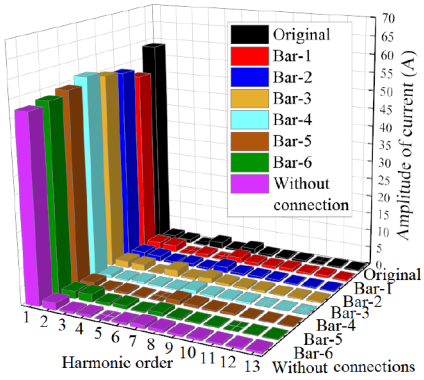

Fig. 15 *Comparison of harmonic components superimposed on armature current under eddy current brake load at average applied voltage 108 V_{rms}*

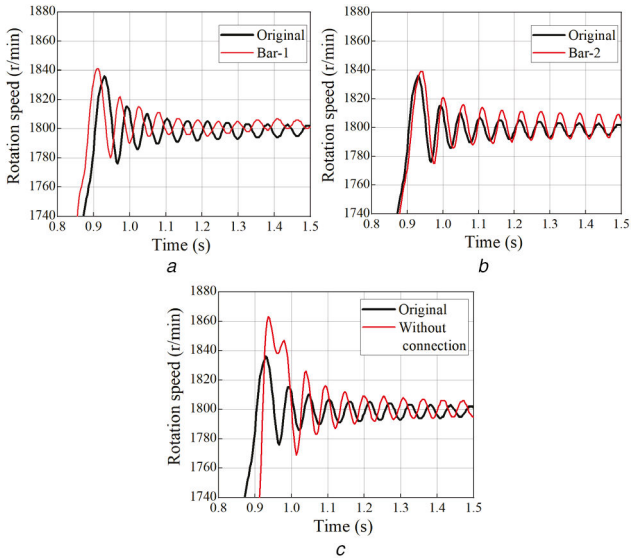

Fig. 16 *Comparison of line-start characteristics with symmetrically changed secondary conductor bar connection under eddy current brake load at average applied voltage 130 V_{rms}*

(a) Original-versus-Bar-1, ***(b)*** Original-versus-Bar-2, ***(c)*** Original-versus-without connection

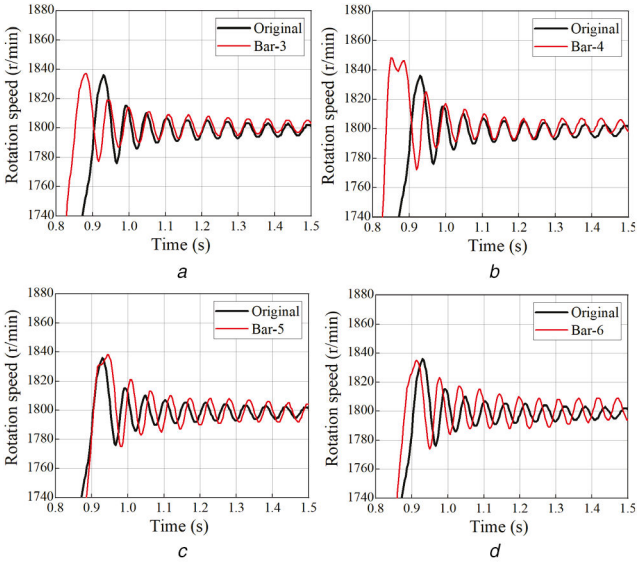

Fig. 17 *Comparison of line-start characteristics with asymmetrically changed secondary conductor bar connection under eddy current brake load at average applied voltage 130 V_{rms}*

(a) Original-versus-Bar-3, ***(b)*** Original-versus-Bar-4, ***(c)*** Original-versus-Bar-5, ***(d)*** Original-versus-Bar-6

increased, the reluctance torque can be synchronised. In this study, it was not possible to measure the current of the secondary conductor bar. In future work, it will be necessary to study the current measurement of the secondary conductor bar and the method of measuring the cross current.

Next, Fig. 22 shows the measured results of the rotor field current. Figs. 22*a* and *b* show the results, when the applied voltage is 102.2 and 132.0 V_{rms}, respectively, with no load. Figs. 22*c* and *d* show the results when the applied voltage is 103.6 and 132.4 V_{rms} for the eddy current brake load, respectively. Here, it is possible to

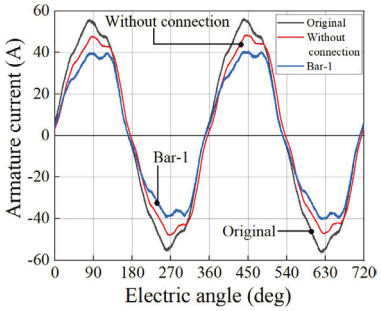

Fig. 18 *Comparison of armature current under eddy current brake load at average applied voltage 130 V_{rms}*

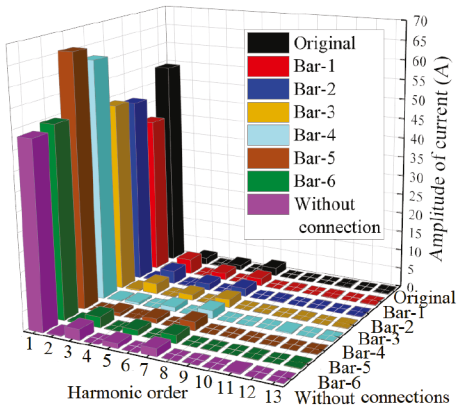

Fig. 19 *Comparison of harmonic components superimposed on armature current under eddy current brake load at average applied voltage 130 V_{rms}*

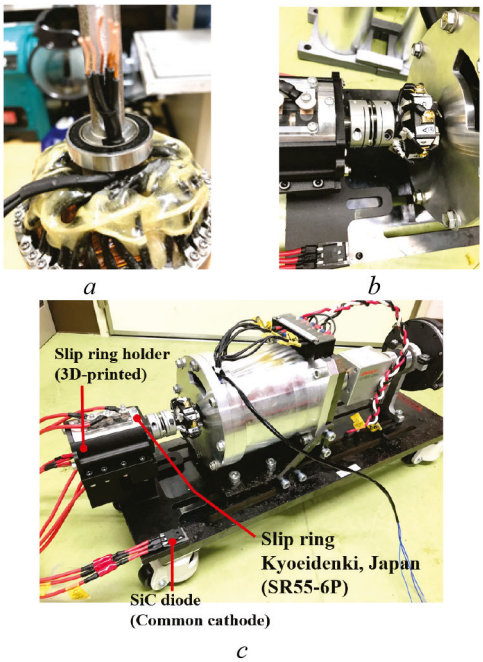

Fig. 20 *Measurement environment for measuring rotor winding current via a slip ring*
(a) Pull out the process of rotor windings, ***(b)*** Relay terminal for connecting slip ring and rotor windings, ***(c)*** Prototype with slipring for rotor current measurement

synchronously pull in all of the conditions in Figs. 22*a–d*. From this figure, it can be seen that the field current is pulsating and composed of a DC component and an AC component of the third harmonic of the fundamental. Fig. 23 shows the measurement results of the armature current and field current from the start to the synchronous pull-in until a steady state is reached. Here, the load is eddy current brake and the applied voltage is 132.1 V_{rms} with secondary conductor bar open model. From this figure, it can be confirmed that the AC components of the field current are generated in the rotor windings. In particular, when the breaker is turned on and the rotor starts to rotate, the large induced current at a slip frequency corresponding to slip $s = 1.0$ flows in the rotor current. In this time, the second space harmonic becomes a second time-harmonic when observed from a stationary rotor. Then, a field current having the slip frequency is generated as the rotation speed increases. Here, the two I-coils connected to the anode of the common cathode diode do not cause the phase difference in the electromotive force, so a large half rectified induced current is generated. This result is useful for considering the difference in the starting characteristics of Figs. 21*c* and *d*. It is considered that the induction torque is generated by the AC component of the field current, so that in Fig. 21*c*, even if the secondary conductor bar is opened, self-starting and synchronous pulling can be performed under no-load condition. It can also be seen that the field current is increasing due to the increase in applied voltage and load. This is because the space harmonics passively increase as the fundamental

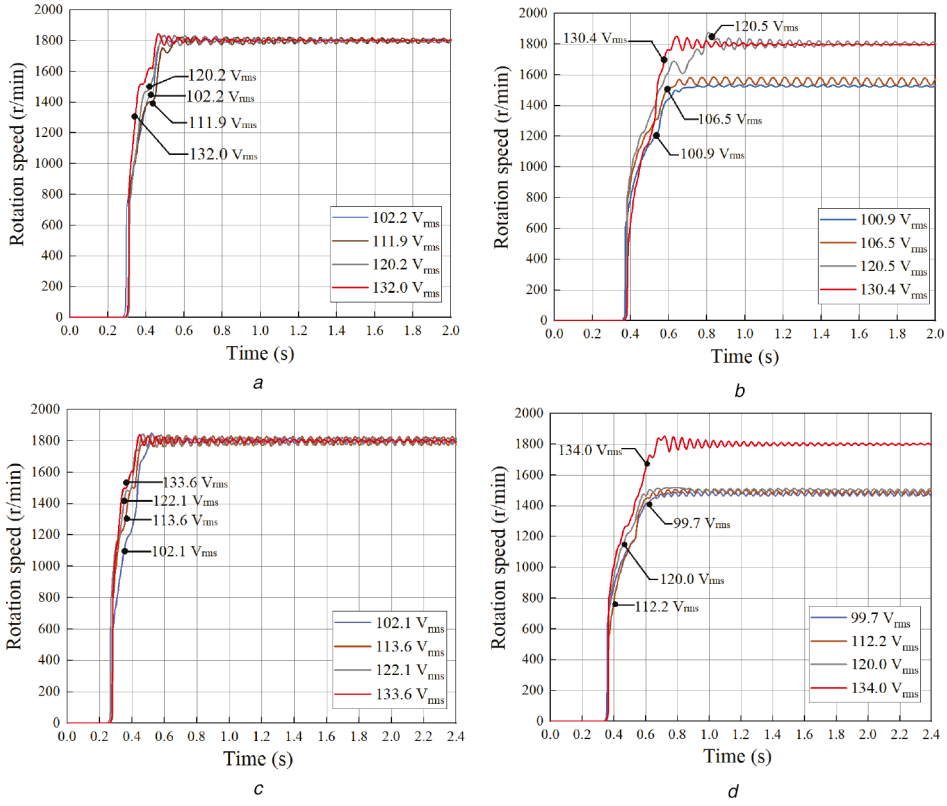

Fig. 21 *Line-start characteristics with respect to applied voltages under no-load*
(a) Original, ***(b)*** With rotor winding open, ***(c)*** With rotor rectifier circuit and without secondary conductor bar connection, ***(d)*** With rotor winding open and without secondary conductor bar connection

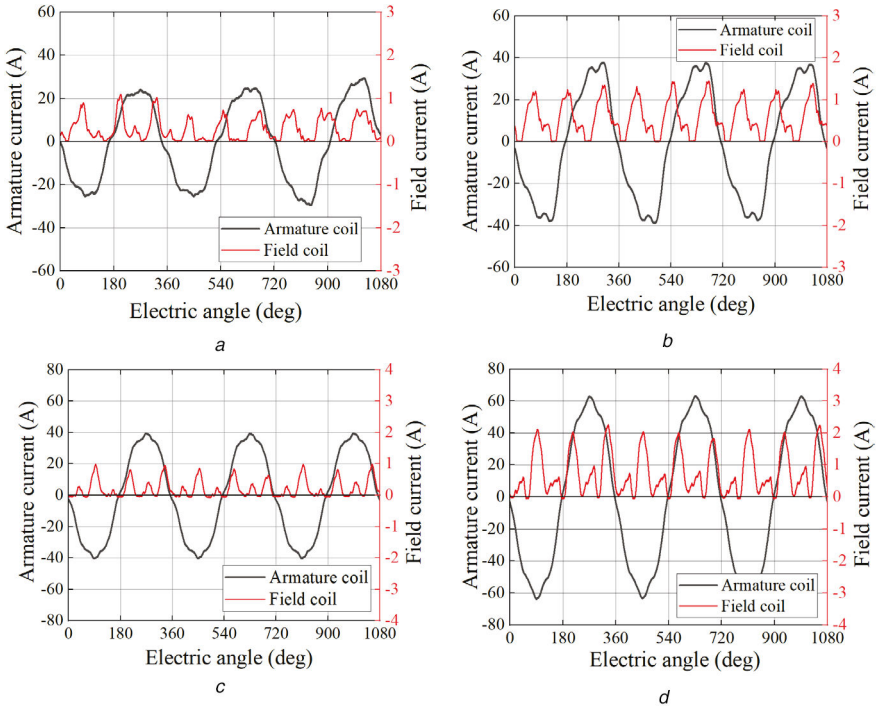

Fig. 22 *Measured U-phase armature current and self-excited rotor field current via a slip ring*
(a) Original under no-load at 102.2 V_{rms}, ***(b)*** Original under no-load at 132.0 V_{rms}, ***(c)*** Original under eddy current brake load at 103.6 V_{rms}, ***(d)*** Original under eddy current brake load at 132.4 V_{rms}

amplitude of the armature current increases. On the other hand, when the amplitude of the armature current in Fig. 23 is confirmed, it reaches 43 A_{rms} immediately after starting and 35 A_{rms} at the steady state. Since the continuous rating during natural air cooling is preferably 8 A/mm^2 or less, the rated current is 4 A_{rms} as shown in Table 1. Therefore, it is about 10.7 times the rated value just after starting, and about 8.7 times the rated value at steady state. In this principle verification machine, the winding inductance was too small, and the result was that the rated current was greatly exceeded. In the future, it will be necessary to optimise the motor parameters and design to meet the required specifications even when directly driven by a commercial three-phase power supply.

Next, in order to verify the effect of the secondary conductor bar on the field current, the rotor field current waveform was

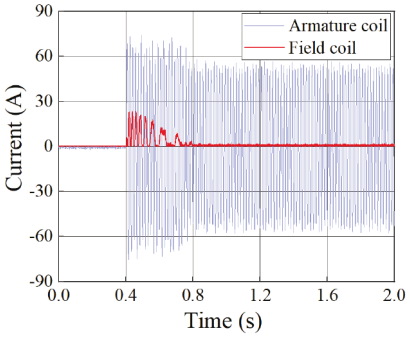

Fig. 23 *Measured armature current and field current from start to steady-state under eddy current brake load at 132.1 V_{rms} with secondary conductor bar open model*

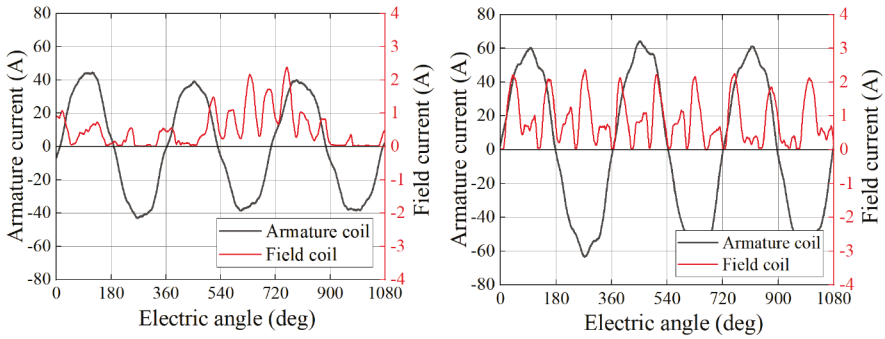

Fig. 24 *Measured U-phase armature current and self-excited rotor field current via a slip ring*
(a) Without secondary conductor bar under no-load at 102.1 V_{rms}, ***(b)*** Without secondary conductor bars under no-load at 133.6 V_{rms}

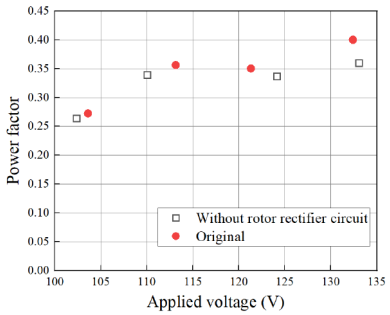

Fig. 25 *Measured power factor with respect to the applied voltage under eddy current brake load*

measured when the secondary conductor bar was opened, and the results are shown in Fig. 24. Under the voltage condition in this figure, both can be synchronised with each other as shown in Fig. 21*c*. Comparing Figs. 24*a* and 22*a* or Figs. 24*b* and 22*b*, it can be confirmed that the rotor field current and the armature current are affected by the connecting of the secondary conductor bar. From these results, not only the starting characteristics differ depending on the secondary conductor bar connection pattern, but also the effect on the amplitude of the self-excited field current and the effect on the harmonic component of the armature current occurs. Since no end-ring is used and the secondary conductor bars are not connected between the poles, stability problems may occur, and the speed ripple may increase. Further, since the connection pattern of the secondary conductor bars also affects the field current ripple in the steady state, there is concern that the torque ripple increases due to the fluctuation of the field flux. It is important to design the slip that maximises the induction torque due to the secondary conductor bars and effectively utilise the induction torque due to the AC component of the field current before synchronisation. After synchronisation, the high secondary conductor resistance may reduce the secondary current and improve the instability problem. On the other hand, at the time of synchronisation, it is necessary to reduce the field current ripple so that only a stable DC current is obtained.

Fig. 25 shows the measured results comparing how the power factor changes by forming the field poles with self-excitation with the original model. From this result, it is understood that the power factor is improved by the organisation of the self-excited field pole. Then, as the applied voltage increases, the power factor improves. This is because the space harmonics that are passively used for self-excitation increase as the armature current increases and the field flux is intensified. Although the power factor value is very low, the motor parameters were not optimised because this prototype was set up for the purpose of principle proof, as described in Section 3.1. In particular, the armature winding inductance and the magnetomotive force balance between the rotor and stator are not optimised. Based on these research results, the motor parameters will be optimised in future works.

3.3 Loss on phase angle during synchronisation

In the line-start type synchronous motor, the phase difference (internal phase difference angle) between the no-load induced voltage and the terminal voltage is an important parameter that determines the machine output. However, in this measurement setup, the rotor position is not acquired, and it is difficult to obtain the internal phase difference angle because of the open-loop drive and the self-excited field pole organisation. Furthermore, since it has a salient pole, it is predicted that the starting characteristics will change depending on the initial position of the rotor. Therefore, the

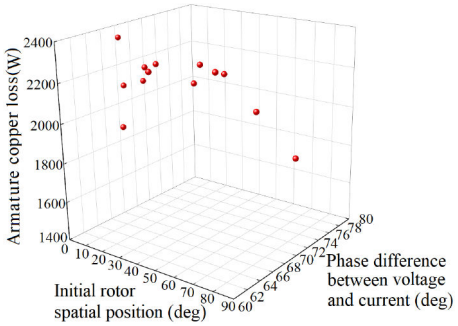

Fig. 26 *Relationship of rotor initial position-versus-voltage and current phase difference-versus-copper loss*

loss evaluation at the time of synchronisation is performed by changing the initial position of the rotor using a digital angle meter. The line voltage and line current are measured using a digital oscilloscope, and the phase voltage and phase current are converted to obtain the phase difference of the fundamental wave. Here, 0°, which is the rotor position reference, is defined at the position where the *N* pole formed by the electromagnet faces the U-phase coil. Fig. 26 shows the graphed results of the relationship between the three parameters of the rotor initial position, the phase difference between the phase voltage and phase current, and copper or iron loss. From Fig. 26, the copper loss tends to increase when the initial position of the rotor is close to 0° and the phase difference between the phase voltage and the phase current is small. From this result, it means that the reluctance torque can be utilised at the same time when the salient pole is provided, but the loss changes depending on the initial position of the rotor so that the balanced design between the loss and the salient pole ratio is important.

4 Conclusion

In this paper, as one of the possibilities of the next-generation line-start type motor, a self-excited wound field synchronous motor with a concentrated winding stator structure capable of line-starting was reported. Regarding the effect of the secondary conductor bars, which has an important effect on the starting characteristics, the starting characteristics were demonstrated by changing the wiring combination using the prototype, and various performances were clarified. Specifically, the following findings were obtained:

(i) The original model has the best starting characteristics, but it is the 'Bar-1' model that can obtain good starting characteristics while suppressing the increase in armature current.
(ii) The damping effect of the secondary conductor bar suppresses the speed ripple from reaching the synchronous speed to the steady state.
(iii) Induction torque is also generated by the AC component of the field current, which contributes to improving the starting characteristics.
(iv) The secondary conductor bar affects the self-excited field current and the armature current by magnetic interference. When optimally designing the secondary conductor bars, it is necessary to evaluate not only the starting characteristics but also harmonic components of field current and armature current and losses.
(v) If insulation is not provided between the secondary conductor bars and the rotor core, a cross current will occur, and induction torque will be generated. However, since the loss will increase, a detailed analysis of the starting characteristics and losses will be required in the future.
(vi) The power factor is improved by forming the self-excited poles.
(vii) The loss differs depending on the initial position of the rotor and the phase difference between the phase voltage and the phase current.

Based on the research results obtained in this paper, future work is planned to perform performance design that meets the IE4 efficiency standard with an industrial general-purpose motor of several kW.

5 References

[1] Boldea, I.: 'Electric generators and motors: an overview', *CES Trans. Electr. Mach. Syst.*, 2017, **1**, (1), pp. 3–14
[2] Ugale, R.T.: 'Overview of research evolution in the field of line start permanent magnet synchronous motors', *IET Electr. Power Appl.*, 2013, **8**, (4), pp. 141–154
[3] Ugale, R.T., Chaudhari, B.N.: 'Rotor configurations for improved starting and synchronous performance of line start permanent-magnet synchronous motor', *IEEE Trans. Ind. Electron.*, 2017, **64**, (1), pp. 138–148
[4] Yan, B., Wang, X., Yang, Y.: 'Parameters determination and dynamic modelling of line-start permanent-magnet synchronous motor with a composite solid rotor', *IET Electr. Power Appl.*, 2019, **13**, (1), pp. 17–23
[5] Ghahfarokhi, M.M., Aliabad, A.D., Boroujeni, S.T., *et al.*: 'Analytical modelling and optimisation of line start LSPM synchronous motors', *IET Electr. Power Appl.*, 2020, **14**, (3), pp. 398–408
[6] Lin, M., Li, D., Zhao, Y., *et al.*: 'Improvement of starting performance for line-start permanent magnet motors by winding reconfiguration', *IEEE Trans. Ind. Appl.*, 2020, **56**, (3), pp. 2441–2450
[7] Takahashi, A., Kikuchi, S., Miyata, K., *et al.*: 'Asynchronous torque of line-starting permanent-magnet synchronous motors', *IEEE Trans. Energy Convers.*, 2015, **30**, (2), pp. 498–506
[8] Tian, M., Wang, X., Wang, D., *et al.*: 'A novel line-start permanent magnet synchronous motor with 6/8 pole changing winding', *IET Trans. Energy Convers.*, 2018, **33**, (3), pp. 1164–1174
[9] Jędryczka, C., Knypiński, Ł, Demenko, A., *et al.*: 'Methodology for cage shape optimization of a permanent magnet synchronous motor under line start conditions', *IEEE Trans. Magn.*, 2018, **54**, (3), pp. 1–4
[10] Lu, W., Zhao, H., Liu, S.: 'Demagnetization conditions comparison for line-start permanent magnet synchronous motors'. 2014 17th Int. Conf. on Electrical Machines and Systems (ICEMS), Hangzhou, 2014, pp. 48–52
[11] Lin, M., Li, D., Ren, X., *et al.*: 'Dual-stator line-start Vernier permanent magnet synchronous machine'. 2019 IEEE Int. Electric Machines & Drives Conf. (IEMDC), San Diego, CA, USA, 2019, pp. 2239–2244
[12] Ustun, O., Bayram, D., Durak, B., *et al.*: 'Comparison of different line start interior permanent magnet synchronous motor types with respect to IE4 efficiency class'. 2017 18th Int. Symp. on Electromagnetic Fields in Mechatronics, Electrical and Electronic Engineering (ISEF), Lodz, Poland, Sep. 14–16, 2017, pp. 1–2
[13] Poudel, B., Amiri, E., Rastgoufard, P.: 'Design and analysis of line start synchronous reluctance motor with dual saliency'. 2018 IEEE Transportation Electrification Conf. and Expo (ITEC), Long Beach, CA, 2018, pp. 385–388
[14] Villani, M., Santececca, M., Parasiliti, F.: 'High-efficiency line-start synchronous reluctance motor for fan and pump applications'. 2018 XIII Int. Conf. on Electrical Machines (ICEM), Alexandroupoli, 2018, pp. 2178–2184
[15] Mingardi, D., Bianchi, N.: 'Line-start PM-assisted synchronous motor design, optimization, and tests', *IEEE Trans. Ind. Electron.*, 2017, **64**, (12), pp. 9739–9747
[16] Liu, H., Lee, J.: 'Optimum design of an IE4 line-start synchronous reluctance motor considering manufacturing process loss effect', *IEEE Trans. Ind. Electron.*, 2018, **65**, (4), pp. 3104–3114
[17] Castagnini, A., Känsäkangas, T., Kolehmainen, J., *et al.*: 'Analysis of the starting transient of a synchronous reluctance motor for direct-on-line applications'. 2015 IEEE Int. Electric Machines & Drives Conf. (IEMDC), Coeur d'Alene, ID, 2015, pp. 121–126
[18] Shehata, E.G.: 'Design tradeoffs between starting and steady state performances of line-started interior permanent magnet synchronous motor'. 7th IET Int. Conf. on Power Electronics, Machines and Drives (PEMD 2014), Manchester, 2014, pp. 1–6
[19] Mingardi, D., Bianchi, N., Prè, M.D.: 'Geometry of line start synchronous motors suitable for various pole combinations', *IEEE Trans. Ind. Appl.*, 2017, **53**, (5), pp. 4360–4367
[20] Aliabad, A.D., Ghoroghchian, F.: 'Design and analysis of a two-speed line start synchronous motor: scheme one', *IEEE Trans. Energy Convers.*, 2016, **31**, (1), pp. 366–372
[21] Negahdari, A., Sundaram, V.M., Toliyat, H.A.: 'An analytical approach for determining harmonic cusps and torque dips in line start synchronous reluctance motors'. 2016 IEEE Energy Conversion Congress and Exposition (ECCE), Milwaukee, WI, 2016, pp. 1–6

[22] Aoyama, M., Mizuta, T., Miyama, Y., *et al.*: 'Proposal and experimental verification of line-start self-excited wound-field motor with concentrated winding stator'. IEE Japan Annual Conf. 2020, Tokyo, March 13rd, 2020, 50058, pp. 88–89 (in Japanese)
[23] Nøland, J.K., Evestedt, F., Pérez-Loya, J.J., *et al.*: 'Design and characterization of a rotating brushless outer pole PM exciter for a synchronous generator', *IEEE Trans. Ind. Appl.*, 2017, **53**, (3), pp. 2016–2027
[24] Nøland, J.K., Evestedt, F., Pérez-Loya, J.J., *et al.*: 'Comparison of thyristor rectifier configurations for a six-phase rotating brushless outer pole PM exciter', *IEEE Trans. Ind. Electron.*, 2018, **65**, (2), pp. 968–976
[25] Nøland, J.K., Evestedt, F., Lundin, U.: 'Failure modes demonstration and redundant postfault operation of rotating thyristor rectifiers on brushless dual-star exciters', *IEEE Trans. Ind. Electron.*, 2019, **66**, (2), pp. 842–851
[26] Mi, C., Filippa, M., Shen, J., *et al.*: 'Modeling and control of a variable-speed constant-frequency synchronous generator with brushless exciter', *IEEE Trans. Ind. Appl.*, 2004, **40**, (2), pp. 565–573
[27] Rao, Y.T., Chakraborty, C., Basak, S.: 'Brushless induction excited synchronous generator with induction machine operating in plugging mode', *IEEE Trans. Ind. Appl.*, 2018, **54**, (6), pp. 5748–5759
[28] Chakraborty, C., Rao, Y.T.: 'Performance of brushless induction excited synchronous generator', *IEEE J. Emerg. Sel. Top. Power Electron.*, 2019, **7**, (4), pp. 2571–2582
[29] Bukhari, S.S.H., Sirewal, G.J., Ayub, M., *et al.*: 'A new small-scale self-excited wound rotor synchronous motor topology', *IEEE Trans. Magn.*, 2021, **57**, pp. 1–5 (Early Access)
[30] Aoyama, M., Noguchi, T.: 'Permanent-magnet-free-synchronous motor with self-excited wound-field technique utilizing space harmonics'. 2017 IEEE Applied Power Electronics Conf. and Exposition (APEC), Tampa, FL, 2017, pp. 3187–3194